Journal of Materials Chemistry A

ROYAL SOCIETY OF CHEMISTRY

PAPER

View Article Online
View Journal | View Issue

Cite this: J. Mater. Chem. A, 2025, 13, 4576

Improving nitrate-to-ammonia conversion efficiency on electrodeposited nickel phosphide *via* surface δ-FeOOH modification†

Anelisse B. Silva,[a] Eduardo A. Reis,[bc] Jiajun Hu,[d] Josep Albero,[d] Caue Ribeiro,[cd] Lucia H. Mascaro[a] and Hermenegildo García[*d]

Electrocatalytic nitrate reduction to ammonia is an appealing and promising approach for recovering industry and agricultural wastewater. However, there is a lack of efficient electrocatalysts for NO_3^- conversion at low overpotentials and a range of nitrate concentrations, which could enable nitrogen recovery from various wastewater streams. Here, we report an affordable and efficient electrodeposited amorphous-Ni_3P electrode modified with δ-FeOOH, forming a heterojunction catalyst that efficiently converts nitrate into ammonia. The optimum heterojunction performance achieved a high faradaic efficiency of 98% ± 0.72 at −0.3 V *vs.* RHE with an NH_3 production yield of 8.49 mg h^{-1} cm^{-2}, ranking Ni_3P/δ-FeOOH among the most active electrocatalysts so far reported for this process. Ni_3P/δ-FeOOH showed good stability using ethyl cellulose as a green and fluoride-free binder without losing the superficial modification. Mechanistic studies by *in situ* Raman spectroscopy show that the role of δ-FeOOH is the stabilisation of the NO_x intermediates. At the same time, Ni_3P provides *H species available for NO_x reduction, thus resulting in highly selective NO_3 hydrogenation. In contrast, in the absence of δ-FeOOH, Ni_3P exhibits significantly lower NH_3 faradaic efficiency due to simultaneous H_2 evolution. Therefore, the present results show the synergistic effect between δ-FeOOH and Ni_3P in the electrocatalytic nitrate reduction, with δ-FeOOH playing a crucial role in stabilising the reaction intermediates and enhancing the ammonia selectivity.

Received 29th June 2024
Accepted 2nd January 2025

DOI: 10.1039/d4ta04511d

rsc.li/materials-a

Introduction

Ammonia is one of the essential chemical commodities due to its role as a fertilizer,[1,2] and has been responsible for ensuring the world's food supply since the development of the Haber–Bosch process.[3,4] Also, NH_3 has been considered a potential carbon-free molecule for hydrogen storage[3,5] since it is a hydrogen-derived chemical of known storage and transportation infrastructure.[6,7] However, current ammonia production methods, such as the traditional Haber–Bosch process,[8,9] are energy-intensive and contribute significantly to greenhouse gas emissions. The Haber–Bosch process, for instance, is an N_2-converting process that consumes almost 2% of worldwide fossil energy.[10,11] It is also responsible for ∼2% of the total greenhouse gas emissions, surpassing 2.16 kg of CO_2 per kg of NH_3 produced,[12] emphasising the urgent need for more sustainable and efficient ammonia production methods, such as the one we propose with our modified electrode.

Considering the current and possible future relevance of NH_3, alternative production procedures, particularly related to circular economy and appropriate use of residues, are becoming increasingly important. Wastewater, which is often rich in nitrates (NO_3^-), serves as a significant source of nitrogeneous oxide species. These include industrial wastewater with high nitrate concentrations,[13,14] as well as surface water and underground aquifers with lower nitrate levels from agricultural and biological activity.[8,13,15] Currently, state-of-the-art water treatment involves a denitrification process driven by microorganisms, which convert these nitrates to N_2.[16] Thus, an appealing approach for additional ammonia production by residue valorisation would be the electroreduction of these nitrates.[17] Electrocatalytic NO_3^- reduction (eNitRR) can result in ammonia formation with some N_2 and H_2 evolution.[1,2,9]

Despite being promising, eNitRR is a complex multi-electron reduction process that requires nine protons and eight electrons ($NO_3^- + 9H^+ + 8e^- \rightarrow NH_3 + 3H_2O$), making the kinetics of the process complex.[1,2,18] The parasitic hydrogen evolution

[a]Department of Chemistry, Federal University of São Carlos, Rod. Washington Luiz, Km 235, CEP 13565-905, São Carlos, SP, Brazil
[b]Institute of Chemistry of São Carlos, University of São Paulo, Av. Trab. São Carlense, 400, CEP 13.566-590, São Carlos, SP, Brazil
[c]National Nanotechnology Laboratory for Agribusiness, Embrapa Instrumentation São Carlos, R. 15 de Novembro,1452, CEP 13.560-970, São Carlos, SP, Brazil
[d]Instituto de Tecnologia Química, Consejo Superior de Investigaciones Científicas, Universitat Politecnica de Valencia, Av. De los Naranjos s/n, Valencia, 46022 Spain. E-mail: hgarcia@qim.upv.es

† Electronic supplementary information (ESI) available. See DOI: https://doi.org/10.1039/d4ta04511d

reaction (HER) is a competing reaction that can prevail under certain conditions. Therefore, the catalyst must be selective for NO_3^- reduction, providing the reaction intermediate adequate stabilisation and generating H* on the surface from the water-splitting reaction, avoiding fast H* recombination into H_2.[2,18] Among the earth-abundant metal catalysts, transition metal phosphides (TMPs) have been reported as promising candidates to replace noble metal-based electrocatalysts in several electrocatalytic reactions[19,20] due to the hydrogenase-like catalytic mechanism. TMPs can favour hydrogenation reactions, such as eNitRR, through stabilising H* generated during the Volmer step of the HER.[20,21] Moreover, TMPs have been primarily studied for electrocatalytic responses attributed to their intrinsic d-electron configuration favouring the material's high conductivity[20,22] and stability.[22] However, TMPs frequently exhibit poor faradaic efficiency values at lower overpotential for eNitRR due to the parasitic HER.[23]

Heterojunction engineering can effectively modulate the local electronic structure of TMPs and regulate the H*-adsorption energy.[19,22,24] Iron-modified catalysts have significantly enhanced ammonium conversion rates and selectivity by effectively generating H* (ref. 25) species and suppressing N–N coupling.[26] Recently, FeOOH has exhibited distinct catalytic performance and selectivity for eNitRR. Qu *et al.*[27] reported a detailed investigation into the crystal phase engineering of FeOOH and its electrocatalytic performance for NO_3^- reduction. Based on experimental studies and theoretical calculations, the authors discovered that the δ-FeOOH phase shows a unique behaviour that breaks the scaling relationship between the free energy of $*NO_3$ adsorption and the limiting potential and charge transfer. This specific behaviour derives from the hydrogen bond formation between δ-FeOOH and $*NO_x$ intermediates, selectively enhancing the adsorption of these intermediates, thereby favouring higher ammonia selectivity and ammonia yield rate over the HER.

Inspired by the cited previous report, we report an improved eNitRR heterojunction electrode developed by modifying an electrodeposited Ni_3P electrode with δ-FeOOH nanoplates using ethyl cellulose as a binder. The surface modification with δ-FeOOH was achieved through a two-step process: first, the nanoplates were deposited *via* drop-casting, followed by a low-temperature thermal treatment at 220 °C. This modification successfully modulates the activity of the electrodeposited amorphous Ni_3P, allowing eNitRR to occur at a lower overpotential. Superior performance is achieved by combining the two materials, reaching a faradaic efficiency of 97% and 8.49 mg h^{-1} cm^{-2} NH_3 yield, even without using conductive polymeric binders, and the electrodes exhibited outstanding stability. *In situ* Raman spectroscopy showed that the heterojunction electrode mimics the bimetallic catalytic centre of nitrite reductases, in which the FeOOH is responsible for adsorbing NO_3^- and stabilising the intermediates by forming H-bonds, and Ni_3P provides enough H^+ for the nitrate hydrogenation. Furthermore, by simple preparation and modification, the FeOOH efficiently regulates the H* recombination and avoids excessive H_2 evolution, enhancing the NO_3^- electroreduction.

Experimental

Synthesis of the CFP/Ni_3P electrodes

Ni_3P film electrodeposition was performed in a solution of 0.10 M $NiCl_2 \cdot 6H_2O$, 0.2 M NaCl, and 0.3 M NaH_2PO_2.[20] The pH of the deposition bath was adjusted to 4 by adding a concentrated 2.0 M phosphoric acid solution. Carbon Fiber Paper (CFP) (Thermo Scientific – PTFE treated, TGP-H-60) of 1.0 × 1.5 cm^2 was used as the substrate, and a carbon rod electrode was used as the auxiliary electrode. Before deposition, the carbon paper substrate was cleaned with acetone and Milli-Q water in an ultrasonic bath for 10 min and dried at 60 °C for 2 h. The deposition was performed by cyclic voltammetry in a delimited 1.0 cm^2 area of the carbon paper substrate, scanning from −0.40 V to −1.60 V *vs.* Ag/AgCl ($KCl_{sat.}$) at 50 mV s^{-1} for 80 cycles. After deposition, the nickel phosphide films were rinsed with Milli Q water, dried under argon flow, and stored under vacuum.

Synthesis of the FeOOH lamellar samples

The iron oxide-hydroxide lamellar nanoparticles were prepared using an ultrasound-assisted technique.[28] First, 100 mL of a 2 M KOH solution was added drop-wise to 100 mL of a 50 mM $Fe(NH_4)_2(SO_4)_2 \cdot 6H_2O$ solution. Then, 2.5 mL of H_2O_2 was added, and the mixture was treated in an ultrasonic bath for 15 min. The nanoparticles were filtered and washed with Milli Q water until complete removal of the unreacted material, followed by ethanol washing, and then dried at 60 °C overnight.

Synthesis of the CFP/Ni_3P/δ-FeOOH electrodes

Following the electrodeposition, the amorphous Ni_3P electrode surface was modified by drop-casting a suspension of δ-FeOOH nanoparticles. This suspension was prepared by adding 5 mg of δ-FeOOH in 250 μL of ethylene glycol and 20 μL of a 5% ethyl cellulose solution. The mixture was sonicated for 15 min to ensure uniformity. After drop-casting 10 μL of the iron nanoparticle suspension onto the nickel phosphide films, the electrodes were heated at 220 °C in air for 30 min. Control samples, where the δ-FeOOH sample was directly deposited onto the CFP, were also prepared and labelled as CFP/δ-FeOOH.

Sample characterisation

HRFESEM images, EDS mapping, and spectra of the CFP/Ni_3P and CPF/Ni_3P/δ-FeOOH electrodes were acquired with a ZEISS GeminiSEM 500 coupled with an X-ray detector EDS apparatus. HRTEM analysis was performed using a JEOL JEM2100F with an accelerated voltage of 200 kV. The HRTEM samples were prepared by dropping 20 μL of the material suspension onto the carbon-coated Cu TEM grid. The δ-FeOOH nanoparticle suspension was prepared using 1 mg of the sample in 1 mL of ethanol. The deposited Ni_3P sample was obtained by scratching the CFP/Ni_3P film, suspending the material in 500 μL of ethanol, and applying 20 μL onto the TEM grid. XRD analysis of the δ-FeOOH nanoparticles in powder form, CFP/Ni_3P, and CFP/Ni_3P/δ-FeOOH electrodes was performed using a Cubix-pro

PANalytical diffractometer recording from 10 to 80°. XPS surface analysis of the CFP/Ni_3P and CFP/Ni_3P/δ-FeOOH electrodes was performed on a SPECS spectrometer with a Phoibos 150 MCD-9 detector and an Al X-ray source operating at 200 W. The deconvolution of the elements was performed using Casa XPS software (version 2.3.15). Raman spectra were collected from a freshly prepared electrode surface with a Horiba Jobin Yvon-Labram HR UV-visible-NIR Raman microscope spectrometer using a 514 nm laser.

Electrochemical characterisation

Electrochemical characterisation experiments were performed with a potentiostat/galvanostat Gamry interface 1000 workstation using an H-type cell configuration separated with a 117 Nafion membrane. The electrochemical cell was assembled with Hg/HgO (KOH 1.0 M) and graphite rod electrodes as the reference and counter electrodes. The deposited carbon paper electrodes were directly used as working electrodes with an exposed area of 1 cm^2. Before the electrochemical experiments, the electrodes were pre-activated by applying −10 mA cm^{-2} for 600 s in 1.0 M KOH solution. Linear sweep voltammetry (LSV) curves were recorded at a scan rate of 2 mV s^{-1} from 0.10 to −0.80 V *vs.* RHE without *iR* correction in Ar-purged 1.0 M KOH with the addition of 0.10 M KNO_3. The potentials were corrected using the following equation:

$$E_{(RHE)} = E \text{ vs. } Hg/HgO_{(KOH\ 1.0\ M)} + 0.0592 \times pH + 0.098\ V \quad (1)$$

The double-layer capacitance of the CFP/Ni_3P and CFP/Ni_3P/δ-FeOOH samples was obtained by recording cyclic voltammetry curves with scan rates ranging from 10 to 200 mV s^{-1} to estimate the electrochemical active surface area (ECSA). Electrochemical impedance spectroscopy (EIS) tests were performed at −0.05 V *vs.* RHE from 10 kHz to 0.10 Hz with steps of 10 mV in the 1.0 M KOH and 1.0 M KOH + 0.10 M KNO_3 electrolytes.

Nitrate electrolysis was also performed in an H-type cell. Before each test, the 117 Nafion membranes were boiled in 5% hydrogen peroxide solution, deionised water, and 0.50 M sulfuric acid solution for 1 h in each solution,[9] respectively, and finally rinsed with water. Before the test, the electrochemical cell was purged with Ar (99.99%) for at least 20 min. Constant potential electrolysis experiments were performed for 1 h from −0.10 V to −0.80 V *vs.* RHE for the un-modified CFP/Ni_3P and CFP/Ni_3P/δ-FeOOH electrodes to evaluate the performance of the prepared samples. After electrolysis, the samples from the cathodic and anodic compartments were collected for the ammonia and nitrite quantification. Besides investigating the performance at various applied potentials, studies were conducted to evaluate the catalyst's performance at different nitrate concentrations, optimise the applied potential, and determine the electrolyte pH effect. All the electrolysis tests were performed in triplicate to ensure the results were reliable.

Determination of NH_3

The ammonia yield in the solution was quantified using the colourimetric Indophenol blue method using a Merck Spectroquant® N–NH_4 commercial kit. First, a calibration curve for NH_3 was constructed using reference NH_3 solutions in 1.0 M KOH with the addition of NH_4OH from 0.00 to 3.00 mg L^{-1}. For NH_3 quantification with the commercial kit, 0.60 mL of the NH_4-1 reagent was added to 5.0 mL of electrolyte aliquots, followed by a micro spoon (supplied in the kit) of the NH_4-2 reagent, and the sample was stirred for 5 min. After 10 min, 4 drops of the NH_4-3 reagent were added, and the samples were analysed by UV-Vis spectroscopy (Cary 5 G UV-vis-NIR, Varian) in the range of 500 to 800 nm after 20 min. 200 μL of 1.0 M sulfuric acid solution was added as a pH correction step before ammonia quantification to avoid ammonia leakage from the samples. This pH correction step was also performed for the standard curve construction. The standard curve equation ($y = 0.2707x + 0.02307$, $R = 0.9994$) showed a good linear relationship of the registered absorbance with the ammonia concentration, as demonstrated in Fig. S1.†

Operando Raman spectroscopy

Operando in situ Raman spectroscopy was conducted using a LabRAM HR Confocal Raman Microscope spectrophotometer. The excitation wavelength was 532 nm, and the electrolysis was carried out in a commercial Raman electrochemical flow cell acquired from Redoxme® using KOH 1 M as electrolyte with 0.1 M of KNO_3. The Raman spectra were collected using a working electrode with an active area of 3.5 cm^2, a platinum wire as the counter-electrode, and an Ag/AgCl electrode as the reference electrode. Blank samples were collected for each catalyst, and the reaction intermediates were determined from the difference in spectra between the spectra under electrochemical operation conditions and those of the catalyst.

Results and discussion

Synthesis and structural characterisation

The nickel phosphide films were prepared on carbon fibre paper using a co-deposition method employing $NiCl_2$ and HPO_2^- as precursors. The Ni_3P/δ-FeOOH electrodes were

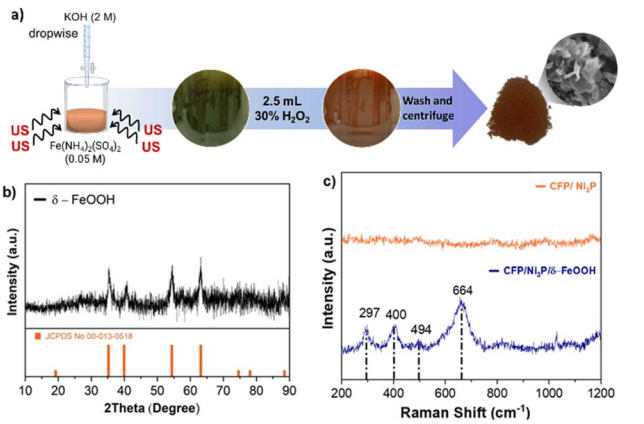

Fig. 1 (a) Schematic diagram of the δ-FeOOH sample synthesis. (b) XRD pattern of the δ-FeOOH sample. (c) Raman spectra of the CFP/Ni_3P and CFP/Ni_3P/δ-FeOOH electrodes.

subsequently prepared by drop-casting the synthesised δ-FeOOH nanoplates on CFP/Ni_3P, as illustrated in Fig. 1a, without any thermal conversion step. The phase structures and crystallinity of the FeOOH sample and the electrodeposited nickel phosphide film were analysed by X-ray diffraction. The FeOOH XRD patterns shown in Fig. 1b reveal the characteristic peaks corresponding to the (100), (002), (102), and (110) planes of the δ-FeOOH phase[29] (JCPDS no. 00-013-0518). From the XRD patterns of the Ni_3P film Fig. S2,† it was possible to index the recorded diffraction peaks of the carbon paper substrate and a broad, weak band between 40° and 60°, indicating the low crystalline nature of the deposited material.[20] After thermal treatment at a low temperature (350 °C under an Ar atmosphere), the XRD pattern of the deposited nickel phosphide (CFP/Ni_3P-TT in Fig. S2†) shows peaks corresponding to the planes (031), (231), (141), and (132) of the Ni_3P crystalline phase in the region of 35°–55°[30] (JCPDS no. 34-0501). Also, diffraction peaks due to metallic Ni were observed due to the low P incorporation capacity of the electrodeposition method.[31,32] Raman spectroscopy analysis was performed to identify further structural differences on the surface of the Ni_3P electrode (Fig. 1c). In addition to the typical bands of the δ-FeOOH pure phase (297, 400, and 664 cm^{-1}),[27,33] a new band at 494 cm^{-1}, assigned to the Ni–O vibration,[34,35] was observed in the modified electrode. It is proposed that Ni–O forms by the interaction of the superficial metallic Ni with iron oxyhydroxide and its partial oxidation during the modification step.

The morphology of the bare (CFP/Ni_3P) and δ-FeOOH-modified nickel phosphide electrodes (CFP/Ni_3P/δ-FeOOH) was analysed by HRFESEM. Fig. 2a and b show that the nickel phosphide film is formed by the growth of spherical microparticles, creating a uniform coating on the carbon fibre paper. SEM images of the δ-FeOOH-modified Ni_3P electrode (Fig. 2d) revealed homogeneously distributed δ-FeOOH nanoplates over the nickel phosphide coating. From higher magnification images in Fig. 2e–f, it is possible to observe that the δ-FeOOH nanoplates cover the granular structure of the nickel phosphide films through weak van der Waals interaction. Elemental mapping analysis of the δ-FeOOH-decorated Ni_3P film (Fig. S3†) demonstrates the homogeneous distribution of Fe, O, Ni, and P in the CFP/Ni_3P/δ-FeOOH electrode.

The structure and morphology of the synthesised δ-FeOOH sample were further analysed by high-resolution transmission electron microscopy (HRTEM). The HRTEM image (Fig. 2g) confirmed the lamellar structure of the δ-FeOOH samples with a nanoplate-like morphology. Lattice fringes observed in Fig. 2h were indexed to δ-FeOOH crystals with d-spacings of 0.23 nm and 0.26 nm for the 002 and 100 facets,[33] confirming the successful preparation of the δ-phase. HRTEM analysis confirms the low crystallinity of the nickel phosphide material, a fact that is commonly observed for electrodeposited metal phosphide films, which present few crystalline micro-regions.[20,32] In the low-crystalline nickel phosphide sample (Fig. 2i), the lattice stripe spacing of 0.246 nm was indexed to the Ni_3P (231) plane, revealing a single-crystalline phase of nickel phosphide. Moreover, HRTEM images of the thermally treated nickel phosphide show the presence of the crystalline micro-regions, which agrees with the XRD pattern, supporting the electrodeposited film's low crystallinity. However, a few crystalline regions can be observed.

X-ray photoelectron spectroscopy (XPS) analysis was performed to study the surface elemental composition of the CFP/Ni_3P/δ-FeOOH electrode. Fig. S4† shows the survey spectrum of the δ-FeOOH-modified Ni_3P electrode, confirming the presence of Ni, Fe, O, and P in the sample. The Ni 2p, P 2p, Fe 2p, and O 1s high-resolution spectra are shown in Fig. 3a–d. In the Ni 2p spectrum, the two spin–orbit coupling peaks ($2p_{3/2}$ and $2p_{1/2}$) of Ni^{2+} are located at 855.3 and 873.1 eV,[36] respectively, accompanied by the two corresponding satellite peaks at 879 and 860.5 eV.[37,38] The doublet peak with a binding energy of 851.2 eV is attributed to the metallic Ni formed by HPO_2^- reduction of

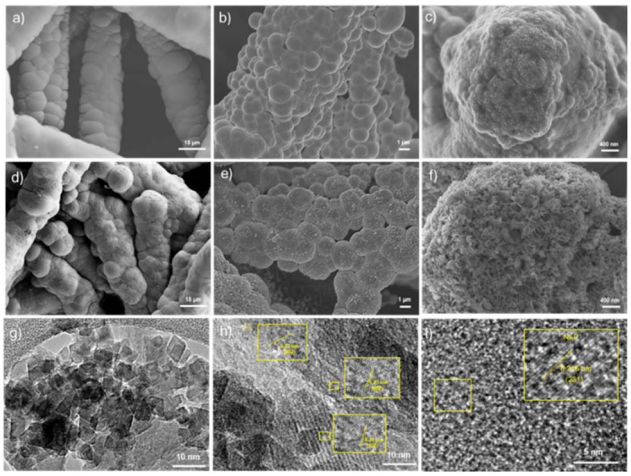

Fig. 2 High-resolution scanning electron microscopy images of the (a–c) CFP/Ni_3P, and (d–f) CFP/Ni_3P/δ-FeOOH samples. (g–i) HRTEM images of the δ-FeOOH and Ni_3P samples.

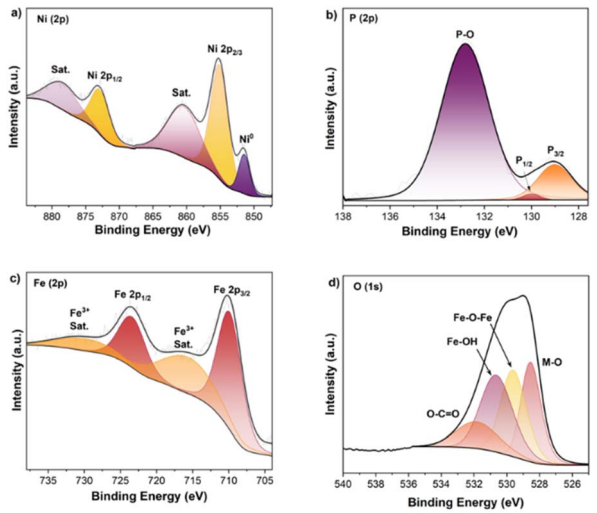

Fig. 3 XPS analysis of the CFP/Ni_3P/δ-FeOOH sample: (a) Ni 2p, (b) P 2p, (c) Fe 2p, and (d) O 1s.

Ni^{2+} on Ni_3P,[37,39] as reported by other authors for Ni_3P samples.[36,39,40]

XPS analysis of the pure Ni_3P with Ar^+ sputtering was also performed (Fig. S5†). The etching process significantly reduced the intensity of the P–O peak in the high-resolution P 2p spectra, confirming that the superficial phosphate phase is primarily a result of air exposure after the electrode preparation. Furthermore, the sharpening of the P–Ni bond peaks in the Ni 2p spectra indicates a predominant presence of Ni–P bonds in the bulk structure, further establishing nickel phosphide as the principal component of the catalyst composition.

The deconvolution of the P spectrum (Fig. 3b) revealed the $2p_{3/2}$ and $2p_{1/2}$ peaks located at 129 and 130.1 eV, which are attributed to Ni–P bonds, thereby supporting the formation of Ni_3P. The presence of the peak at 132.8 eV can be ascribed to the P–O bond commonly formed by surface oxidation due to air exposure. Analysis of the Fe 2p spectrum shows peaks at 723.6 and 709.9 eV, corresponding to $2p_{3/2}$ and $2p_{1/2}$ of Fe^{3+}, with two satellite peaks at 716.5 and 730.6 eV (Fig. 3c).[37,41] The high-resolution spectrum of O 1s (Fig. 3d) of the CFP/Ni_3P/δ-FeOOH electrode was deconvoluted in four distinctive peaks at 532.1, 530.9, 529.8 and 528.8 eV, which can be assigned, respectively, to O–C=O of the ethyl cellulose, Fe–OH, and Fe–O–Fe species of the δ-FeOOH,[42,43] and M–O. The last peak can be attributed either to the Fe–O for the δ-FeOOH surface or the superficial Ni–O formed due to the interaction of Ni with the iron oxyhydroxide[44,45] and the partial oxidation of superficial Ni metallic species during the modification with FeOOH.

eNitRR performance

The eNitRR experiments were carried out in an H-type cell under ambient conditions. The electrocatalytic activity of the electrodeposited electrodes was primarily evaluated by recording LSV polarisation curves without *iR* correction in 1.0 M KOH with and without the addition of 0.1 M KNO_3. Fig. 4a presents a pronounced increase in the current density and a significant shift in the onset potential with KNO_3 addition for all the evaluated electrodes. In contrast, the carbon paper showed a negligible increase, indicating poor catalytic activity for nitrate reduction and confirming that the activity is related to the electrocatalysts. The individual Ni_3P and δ-FeOOH electrodes presented distinct electrochemical behaviour upon incorporating nitrate ions in the solution. The Ni_3P electrode displays a much higher current density than the δ-FeOOH sample. However, the positive shift at onset potential is not as significant as in the δ-FeOOH electrode, suggesting different selectivity for the eNitRR. In the absence of nitrate in the electrolyte, dashed lines in Fig. 4a indicate that the individual CFP/Ni_3P electrode shows the best performance for the HER with an overpotential for -10 mA cm^{-2} of -165 mV that is smaller than -240 mV for the CFP/Ni_3P/δ-FeOOH electrode. The bare δ-FeOOH electrode shows the worst performance for the HER, usually expected for oxyhydroxides due to the stronger hydrogen bonding with the surface O–H, leading to slow H_2 evolution kinetics.[46–49] Compared with the individual samples, the CFP/Ni_3P/δ-FeOOH electrode showed the most enhanced current

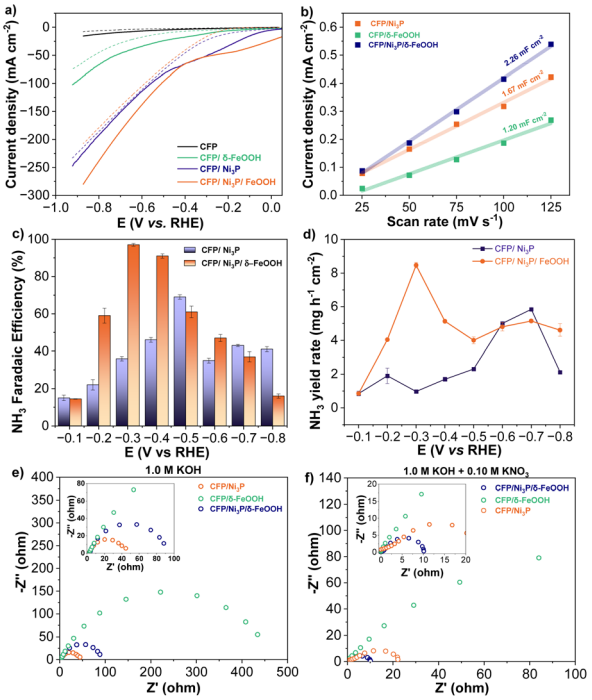

Fig. 4 eNitRR performance: (a) linear sweep voltammetry (at 5 mV s^{-1}) 1.0 M KOH with and without 0.10 M KNO_3 of bare CFP, CFP/δ-FeOOH, CFP/Ni_3P and CFP/Ni_3P/δ-FeOOH. (b) Potential dependent faradaic efficiency and (c) NH_3 yield rate for the bare Ni_3P and the δ-FeOOH modified Ni_3P electrode. (d) Linear regression of the experimental data of charging current *vs.* scan rate obtained by the capacitance method for ECSA estimation. EIS plots for δ-CFP/FeOOH, CFP/Ni_3P, and CFP/Ni_3P/δ-FeOOH in 1 M KOH electrolyte (e) without NO_3^- and (f) with 0.1 M NO_3^-.

density in the KOH + KNO_3 electrolyte and a more significant positive shift of the onset potential, suggesting a superior catalytic ability for the nitrate conversion.

Double-layer capacitance (C_{dl}) values were estimated (Fig. 4b) to understand the synergistic effect of the addition of δ-FeOOH nanoplates on the electrochemically active surface area (ECSA) of the Ni_3P electrode. From the estimated C_{dl} values shown in Fig. 4b, the ECSA of the modified CFP/Ni_3P/δ-FeOOH (55 cm^2) electrode was more prominent than for the separate CFP/Ni_3P (41.7 cm^2) and CFP/δ-FeOOH (30 cm^2) electrodes, revealing that the integration of both catalysts in the CFP/Ni_3P/δ-FeOOH electrode increased the number of active sites for the eNitRR.[50] The ECSA-normalized polarisation curves in Fig. S6† demonstrate that the CFP/Ni_3P/δ-FeOOH electrode achieves a higher current density in the evaluated potential range and, hence, a superior inherent activity.

Continuous nitrate electrolysis experiments were performed for potentials ranging from -0.10 to -0.80 V *vs.* RHE to optimise the performance for ammonia production. Fig. 4c and d display the potential-dependent faradaic efficiencies and ammonia yield rates for the un-modified and δ-FeOOH-modified Ni_3P electrodes. The corresponding chronoamperometry curves are shown in Fig. S7.† The bare Ni_3P sample achieves a faradaic efficiency of 69.0 ± 1.2% (-0.50 V *vs.*

RHE) with a maximum ammonia yield rate of 5.84 mg h^{-1} cm^{-2} at −0.70 V *vs.* RHE. Meanwhile, the CFP/Ni_3P/δ-FeOOH electrode exhibited an optimum performance with a higher faradaic efficiency peak of 98.0 ± 0.7% at a low overpotential of −0.3 V *vs.* RHE and NH_3 production yield of 8.49 mg h^{-1} cm^{-2}, therefore, indicating not only a different catalytic activity tendency for the δ-FeOOH-modified Ni_3P electrode but also an enhanced ammonia selectivity for this modified electrode, as can be seen in the faradaic efficiency. The modified Ni_3P electrode enhances the efficiency of energy (or charge) utilisation for ammonium production, achieving a higher yield with reduced energy consumption.

Nitrite is undesirably obtained as a byproduct of the direct electrochemical nitrate reduction reaction. After electrolysis, the nitrite (NO_2^-) content was also quantified using the standard electroanalytical method (Fig. S8†). Fig. S9† shows the variation of the faradaic efficiency for the co-product nitrite within the applied potential. Although the nitrite faradaic efficiency at −0.10 V *vs.* RHE is higher than 10% for both electrodes, the CFP/Ni_3P/δ-FeOOH electrode showed a greater decreasing tendency for more negative applied potentials than the CFP/Ni_3P electrode. In both cases, the decline in the nitrite faradaic efficiency was accompanied by a significant increase in the ammonia faradaic efficiency and ammonia yield rate, demonstrating that the nitrate conversion to ammonia is the more selective process for the deposited electrodes. Control experiments of the individual CFP and CFP/δ-FeOOH electrodes were conducted to rule out possible sources of external contamination and verify their contribution to the catalytic performance (Fig. S10†).

In comparison with the Ni_3P-containing electrodes, the bare CFP/δ-FeOOH showed the lowest reduction ability at −0.30 V *vs.* RHE with a low faradaic efficiency for ammonia production of 30.0% ± 0.5 and the lowest ammonia yield of 0.25 mg h^{-1} cm^{-2}. In addition, the bare carbon fibre paper showed a negligible ammonia yield. The developed electrode outperformed most electrocatalysts reported in the literature for alkaline nitrate electroreduction to ammonia[51] regarding faradaic efficiency and NH_3 yield rate achieved with low overpotential values, see Fig. S11.†

Furthermore, the influence of the δ-FeOOH modification on the Ni_3P electrodes in the kinetics of the samples was studied by electrochemical impedance spectroscopy (EIS) analysis in the presence and absence of nitrate ions. Fig. 4e and f show the Nyquist plots recorded at −0.05 V *vs.* RHE corresponding to the 1.0 M KOH and 1.0 M KOH + 0.10 M KNO_3 electrolytes, respectively. The HER takes place with no nitrate, and the charge transfer resistance mediates the reaction on the electrode surface by reducing the water molecule.[52,53] As one can see, the CFP/Ni_3P electrode exhibits the smallest semicircle in the 1.0 M KOH electrolyte compared to the CFP/δ-FeOOH and CFP/Ni_3P/δ-FeOOH and electrodes, indicating a better charge transport to promote H_2 production and hence a better HER performance. Fig. 4f provides the Nyquist plots of the prepared electrodes after introducing the NO_3^- ions in the electrolyte in which the nitrate reduction reaction and hydrogen evolution reaction co-occur. In this case, there is a catalytic behaviour switch, and a smaller semicircle is observed for the CFP/Ni_3P/δ-FeOOH, which indicates faster transfer kinetics for the eNitRR. The effect is also observed for the Ni_3P electrode, which, despite lower charge transfer resistance than the CFP/δ-FeOOH sample, is still higher than that of the heterojunction. These results indicate that the incorporation of the δ-FeOOH nanoplates leads to faster kinetics for the nitrate ion conversion over the HER and a slightly higher ECSA, which are responsible for the superior catalytic activity observed for the CFP/Ni_3P/δ-FeOOH electrode at low overpotential value.

The developed heterojunction was tested for the eNitRR in different nitrate concentrations to investigate the applicability of the electrocatalyst. The concentrations of 0.005, 0.025, 0.050, 0.075, and 0.10 M of NO_3^- were chosen because they cover the range of the nitrogen oxide ions (NO_3^- and NO_2^-) contained in industrial wastewater and contaminated groundwater.[54–56] LSV curves for the CFP/Ni_3P/δ-FeOOH under the various nitrate concentrations are presented in Fig. S12a.† As verified, the introduction of higher nitrate concentration in the electrocatalytic system implied a positive shift in the overpotential with a significant increase in current density, indicating that the CFP/Ni_3P/δ-FeOOH sample possesses the ability to catalyse the nitrate reduction at different nitrate concentrations. From the ammonia production rates and faradaic efficiencies presented in Fig. S12b,† it is verified that both factors gradually increase with the concentration of nitrate ions in the electrolyte. Although a decrease in the faradaic efficiency is observed in the lowest nitrate concentration, the ammonia production rate, 1.1 mg h^{-1} cm^{-2}, is comparable to some catalysts[54,57–60] reported in an alkaline medium with 20 times higher NO_3^- concentration and usually more negative applied overpotential. Therefore, these numbers at mM NO_3^- concentration show the superior performance of CFP/Ni_3P/δ-FeOOH and open the possible applicability of the electrode to industrial wastewaters.

Stability performance

Consecutive cycling of eNitRR was performed under the optimised conditions to evaluate the stability of the heterojunction electrocatalyst prepared with natural cellulose as the binder (Fig. 5). Surprisingly, the catalyst resisted more than ten catalytic cycles, retaining the high NH_3 yield and faradaic efficiency (~94% F.E. was retained).

Moreover, the simple and fluoride-free preparation of the electrode demonstrated excellent stability during startup and shutdown cycles, suggesting that this modification strategy is promising for producing durable catalysts. However, further long-term performance evaluations are necessary to assess its viability for practical applications. Compared with the literature, the electrode exhibited similar stability behaviour to the self-supported catalyst[61–64] and superior electrochemical stability to electrodes prepared using synthetic polymers such as Nafion[27,60,65,66] and poly(methyl methacrylate) (PMMA).[67]

In addition, XPS data were further collected from the CFP/Ni_3P/δ-FeOOH electrode after the ten consecutive cycling tests to investigate the catalyst stability and the chemical states. For the Fe 2p region (Fig. 5b), the same peaks corresponding to Fe^{3+}

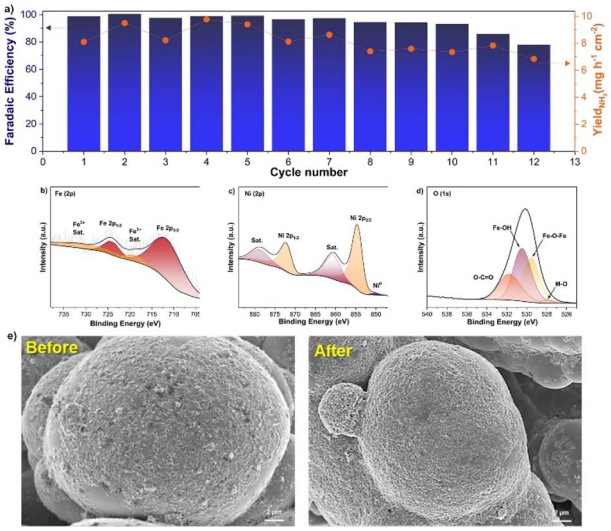

Fig. 5 (a) Consecutive recycling test of the CFP/Ni_3P/δ-FeOOH electrode at −0.3 V *vs.* RHE. XPS spectra of the CFP/Ni_3P/δ-FeOOH sample after 10 consecutive recycling cycles: (b) Fe 2p, (c) Ni 2p, and (d) O 1s. (e) High-resolution scanning electron microscopy images of the CFP/Ni_3P/δ-FeOOH sample freshly prepared and after the recycling cycles.

are identified as in the previous characterisation (Fig. 3c) without indicating the reduction of the superficial iron valence state. Only a slight decrease in the intensity is observed, probably due to the partial FeOOH restructuration over time, and the catalyst activity remains almost the same, demonstrating that only a low amount of iron oxyhydroxide is restructured and the cellulose efficiently retains the FeOOH on the surface of the Ni_3P. The spectrum of Ni 2p (Fig. 5c) shows a change in the peak intensity at ~851 eV, referring to $Ni^{\delta+}$ from metal species, due to the surface reconstruction already observed for nickel phosphide at long-term operation in alkaline medium.[35,68] No changes in the other peaks were observed, indicating no surface P leaching. However, due to the startup and shutdown cycles, an oxidation process is observed in the P 2p spectra for the superficial phosphide (Fig. S13†). As already described in the literature, the superficial metallic Ni and FeOOH generally suffer from reconstruction during the consecutive cycling process in an alkaline medium and produce an iron-nickel phase.[49,69,70] Another peak intensity change is observed in Fig. 5d for the O 1s region. The intensity of the Fe–O–Fe peak is weakened, confirming the restructuration of the δ-FeOOH. However, a considerable amount of δ-FeOOH nanoplates stays on the Ni_3P surface, as shown in the HRSEM image (Fig. 5d and e). Furthermore, the intensity of the M–O peak becomes relatively weak due to the reconstruction of δ-FeOOH and Ni^0 on the surface since this peak can be associated with the Fe–O and the Ni–O formed during the electrode modification step.

Structural dynamics and active site investigation of CFP/Ni_3P/δ-FeOOH

Electrochemical *in situ* Raman spectroscopy were performed to investigate the selectivity change in the nitrate reduction process with the δ-FeOOH modification on the Ni_3P surface. *In situ* Raman tests were conducted at open circuit potential (OCP) and under optimal eNitRR conditions for CFP/Ni_3P/δ-FeOOH (−0.3 V *vs.* RHE with 0.1 M KNO_3) to determine the reaction intermediate formation. The Raman spectra were collected 20 min after the start of the electroreduction reaction at a constant potential to detect the intermediates on the catalyst surface. For both catalysts, with and without the FeOOH modification, a decrease in the intensity of the NO_3^- stretch peak in solution[71–73] located at 1048 cm^{-1} can be observed in Fig. 6a, showing that even without modification, the Ni_3P can reduce nitrate in alkaline solutions. Meanwhile, a broad feature from 800–950 cm^{-1} appears with the potential applied, corresponding to the H* adsorbed from the water dissociation.[74] For the δ-FeOOH modified Ni_3P, it is observed that the broad feature exhibits lower Raman intensity, which indicates that the presence of δ-FeOOH on the Ni_3P surface limits the H* generation and balances the generation of active hydrogen for efficient nitrate reduction, avoiding H_2 evolution by the excess formation of adsorbed H*. In the pure Ni_3P Raman spectra, there is evidence for the formation of the HNO intermediate around 1529 cm^{-1} that can be related to the N=O stretch of HNO,[75] implying that the adsorbed NO is converted to HNO even in an alkaline environment due to the local acidic-like environment near the electrode surface and the presence of

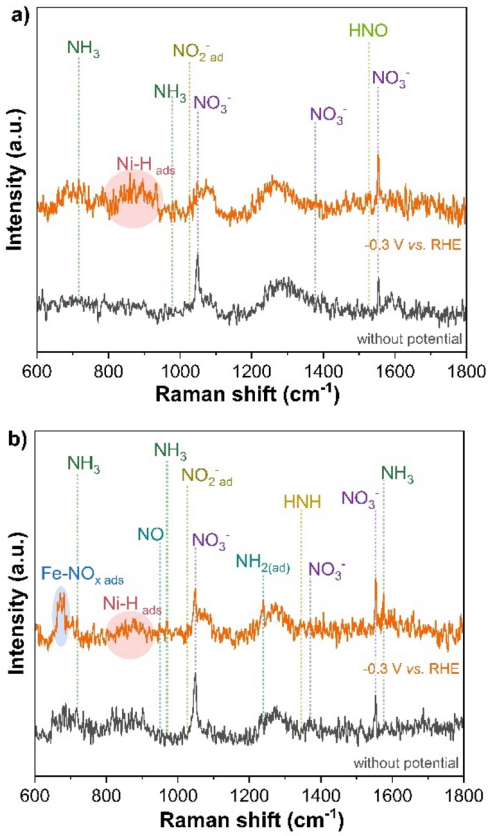

Fig. 6 *Operando* Raman spectra without applied potential and at −0.3 V *vs.* RHE for (a) CFP/Ni_3P and (b) CFP/Ni_3P/δ-FeOOH.

adsorbed H* from the HER,[76] which is usually observed for the Ni-based catalyst.[48,77,78]

Although the HNO intermediate can be detected in the Ni_3P Raman spectra, only low-intensity peaks associated with NH_3 can be identified at 714 cm^{-1} (ref. 71 and 75) and 974 cm^{-1} (ref. 79), and the peak for the NH_3 linked to the catalyst surface at 1574 cm^{-1} corresponding to the NH_3 asymmetric bending[73,80] is not seen. These results agree with the lower F.E. and NH_3 production yield for pure Ni_3P catalysts, indicating low ammonia production selectivity. In contrast, after the modification, more intense peaks for NH_3 were observed, with the most prominent peak at 1575 cm^{-1} that can be assigned to the antisymmetric H–N–H deformation mode of the NH_3 linked to the Fe sites with Lewis acid character.[75,80] Other intense peaks are seen at 714 cm^{-1} and 1350 cm^{-1}, related to the rocking vibrations[81] and HNH deformation of the NH_3,[71,80] respectively. Furthermore, two new peaks can be observed at 1235 cm^{-1} and 950 cm^{-1}, both associated with the adsorbed intermediate NH_2OH on the δ-FeOOH surface,[73,82] which agrees with the information offered by online DEMS in a previous report for FeOOH phases,[27] indicating a change in the mechanism of nitrate reduction with the modification. In addition, when the potential is applied, a new broad and intense peak appears around 664 cm^{-1}, possibly related to the coordination of Fe–NO_x,[83–87] which shows a Raman shift between 570 and 660 cm^{-1} in comparison to nitroxyl and heme complexes due the stabilisation of the NO_x intermediate (*NO, *NO_2, and *NO_3) by the hydrogen bond[88,89] between the hydroxyl groups exposed on the FeOOH and the oxygen atoms present in the nitrate intermediate. Based on the *in situ* Raman analysis for the pure Ni_3P, the H_2 evolution reaction prevails over the NO_3^- reduction. The HER in an alkaline medium usually takes place through the Volmer and Heyrovsky steps:

$$H_2O + e^- \rightarrow *H + HO^- \text{ (Volmer step)}$$

$$*H + H_2O + e^- \rightarrow H_2 + HO^- \text{ (Heyrovsky step)}$$

It should be noted that after the modification with δ-FeOOH, the reaction selectivity changes from the HER to eNitRR. The primary role of the Ni_3P appears to be the generation of adsorbed H* by dissociating H_2O (Volmer step) to provide enough available surface hydrogen for the hydrogenation of NO_3^- rather than the reduction of H_2O, thus leading to NH_3 instead of H_2. The role of the iron oxyhydroxide would be, on the other hand, aside from stabilising the Fe–NO_x intermediate, the inhibition of hydrogen evolution (Heyrovsky step) by favouring NH_3. The enhanced NO_3^- selectivity can be attributed to the "relay catalytic effects"[90] in the adjacent FeOOH and Ni_3P catalytic sites, with FeOOH promoting the adsorption and activation of NO_3^- and the NO_x intermediates and the Ni sites lowering the reaction barrier, promoting the hydrogenation of the adsorbed intermediates. Also, in the modified electrode, Ni_3P enhances the charge transfer mechanism between the active sites and adsorbed intermediates, lowering the electron migration to the eNitRR intermediate.[91–93]

Conclusions

We demonstrated that CFP/Ni_3P/δ-FeOOH heterojunctions are efficient electrocatalysts for nitrate conversion to ammonia, with low potential and capable of operating under low NO_3^- concentration conditions. Modifying the Ni_3P electrodeposited electrode surface with the δ-FeOOH nanoplates hinders the HER by adsorbing NO_x species that consume adsorbed *H, minimising their excess and thereby increasing the ammonia production rate and the faradaic efficiency. The superficial modification treatment depositing an active δ-FeOOH nanoplate material improved the NO_3^- active sites, promoting an increase in the ECSA of the electrodeposited Ni_3P. Electrochemical *in situ* Raman spectroscopy analysis indicates that the role of nickel phosphide during the eNitRR changes after the modification. We observed that iron oxyhydroxide facilitates NO_3^- adsorption, at the same time that its structure stabilises the NO_x intermediates, while the principal role of Ni_3P is to provide adsorbed *H from the water-splitting reaction available for NO_x reduction.

Furthermore, the heterojunction catalyst resisted more than ten consecutive cycles of NitRR, showing good stability over the startup and shutdown cycles while retaining the high NH_3 yield and faradaic efficiency (~94% F.E. was retained) even without synthetic polymer binders. The electrode also delivers an excellent faradaic efficiency yield with substantial NH_3 production even at 5 mM NO_3^- concentration. This work shows the potential application of the CFP/Ni_3P/δ-FeOOH catalyst for NH_3 electrosynthesis and a feasible alternative for modifying the activity and selectivity of electrodeposited metal phosphide electrodes and modulating their activity.

Data availability

Data are available from the corresponding authors upon reasonable request.

Author contributions

Anelisse B. Silva: investigation, writing – original draft. Eduardo Arizono dos Reis: investigation, writing – original draft. Jiajun Hu: investigation. Josep Albero: investigation, writing – review & editing. Lucia Helena Mascaro: resources, review & editing. Caue Ribeiro: conceptualization, writing – review & editing. Hermenegildo Garcia: supervision, writing – review & editing, resources, conceptualisation.

Conflicts of interest

There are no conflicts to declare.

Acknowledgements

The authors are grateful for the sponsorship and financial support of FAPESP (#2017/11986-5, #2018/01258-5, #2020/11756-2, #2022/15742-1, #2021/12394-0 and # 2013/07296-2), Coordenação de Aperfeiçoamento de Pessoal de Nível

Superior – Brazil (CAPES) – Finance Code 001, Conselho Nacional de Desenvolvimento Científico e Tecnológico, CNPq, grant number #152607/2022-6, #311769/2022-5, #405133/2023 and #406156/2022-0, and FINEP-Financiadora de Estudos e Projetos grant number #01.22.0179.00, #01.23.0645.00. Also financial support from the Spanish Ministry of Science and Innovation (CEX-2021-001230 S and PDI2021-0126071-OB-CO21 funded by MCIN/AEI/10.13039/501100011033) and Generalitat Valenciana (Prometeo 2021/038 and Advanced Materials programme Graphica MFA/2022/023 with funding from European Union NextGenerationEU PRTR-C17.I1) is gratefully acknowledged.

References

1 L. Sun and B. Liu, *Adv. Mater.*, 2023, **35**, 2207305.
2 H. Zhang, H. Wang, X. Cao, M. Chen, Y. Liu, Y. Zhou, M. Huang, L. Xia, Y. Wang, T. Li, D. Zheng, Y. Luo, S. Sun, X. Zhao and X. Sun, *Adv. Mater.*, 2024, **36**, 2312746.
3 G. Chehade and I. Dincer, *Fuel*, 2021, **299**, 120845.
4 J. W. Erisman, M. A. Sutton, J. Galloway, Z. Klimont and W. Winiwarter, *Nat. Geosci.*, 2008, **1**(10), 636–639.
5 S. Ghavam, M. Vahdati, I. A. G. Wilson and P. Styring, *Front. Energy Res.*, 2021, **9**, 580808.
6 K. Adeli, M. Nachtane, A. Faik, D. Saifaoui and A. Boulezhar, *Appl. Sci.*, 2023, **13**, 8711.
7 N. Salmon, R. Reń, R. Bã Nares-Alcántara and A. Alcántara, *Sustain. Energy Fuels*, 2021, **5**, 2814–2839.
8 L. X. Li, W. J. Sun, H. Y. Zhang, J. L. Wei, S. X. Wang, J. H. He, N. J. Li, Q. F. Xu, D. Y. Chen, H. Li and J. M. Lu, *J. Mater. Chem. A*, 2021, **9**, 21771–21778.
9 G. F. Chen, Y. Yuan, H. Jiang, S. Y. Ren, L. X. Ding, L. Ma, T. Wu, J. Lu and H. Wang, *Nat. Energy*, 2020, **5**(8), 605–613.
10 M. Capdevila-Cortada, *Nat. Catal.*, 2019, **2**(12), 1055.
11 X. Liu, A. Elgowainy and M. Wang, *Green Chem.*, 2020, **22**, 5751–5761.
12 S. Ghavam, C. M. Taylor and P. Styring, *Front. Energy Res.*, 2021, **9**, 600071.
13 J. Theerthagiri, J. Park, H. T. Das, N. Rahamathulla, E. S. F. Cardoso, A. P. Murthy, G. Maia, D.-V. N. Vo and M. Y. Choi, *Environ. Chem. Lett.*, 2022, **20**(5), 2929–2949.
14 C. Lv, L. Zhong, Y. Yao, D. Liu, Y. Kong, X. Jin, Z. Fang, W. Xu, C. Yan, K. N. Dinh, M. Shao, L. Song, G. Chen, S. Li, Q. Yan and G. Yu, *Chem*, 2020, **6**, 2690–2702.
15 R. Jia, Y. Wang, C. Wang, Y. Ling, Y. Yu and B. Zhang, *ACS Catal.*, 2020, **10**, 3533–3540.
16 S. Huang, Y. Fu, H. Zhang, C. Wang, C. Zou and X. Lu, *Front. Microbiol.*, 2023, **14**, 1284369.
17 N. Zhang, G. Zhang, P. Shen, H. Zhang, D. Ma and K. Chu, *Adv. Funct. Mater.*, 2023, **33**, 2211537.
18 O. Peng, Q. Hu, X. Zhou, R. Zhang, Y. Du, M. Li, L. Ma, S. Xi, W. Fu, Z. X. Xu, C. Cheng, Z. Chen and K. P. Loh, *ACS Catal.*, 2022, **12**, 15045–15055.
19 Z. Pu, T. Liu, I. S. Amiinu, R. Cheng, P. Wang, C. Zhang, P. Ji, W. Hu, J. Liu and S. Mu, *Adv. Funct. Mater.*, 2020, **30**, 2004009.
20 A. B. Silva, M. Medina, L. A. Goulart and L. H. Mascaro, *Electrochim. Acta*, 2024, **475**, 143679.
21 T. Chouki, M. Machreki, I. A. Rutkowska, B. Rytelewska, P. J. Kulesza, G. Tyuliev, M. Harb, L. M. Azofra and S. Emin, *J. Environ. Chem. Eng.*, 2023, **11**, 109275.
22 L. Wang, N. Gong, Z. Zhou, W. Peng, Y. Li, F. Zhang and X. Fan, *Int. J. Hydrogen Energy*, 2022, **47**, 18305–18313.
23 J. Hu, H. Huang, M. Yu, S. Wang and J. Li, *Nano Res.*, 2024, **17**, 4864–4871.
24 Q. Zhou, L. Liao, Q. Bian, F. Yu, D. Li, J. Zeng, L. Zhang, H. Wang, D. Tang, H. Zhou and Z. Ren, *Small*, 2022, **18**, 2105642.
25 R. Zhang, Y. Guo, S. Zhang, D. Chen, Y. Zhao, Z. Huang, L. Ma, P. Li, Q. Yang, G. Liang and C. Zhi, *Adv. Energy Mater.*, 2022, **12**, 2103872.
26 Z. Y. Wu, M. Karamad, X. Yong, Q. Huang, D. A. Cullen, P. Zhu, C. Xia, Q. Xiao, M. Shakouri, F. Y. Chen, J. Y. (Timothy) Kim, Y. Xia, K. Heck, Y. Hu, M. S. Wong, Q. Li, I. Gates, S. Siahrostami and H. Wang, *Nat. Commun.*, 2021, **12**(1), 1–10.
27 K. Qu, X. Zhu, Y. Zhang, L. Song, J. Wang, Y. Gong, X. Liu and A. L. Wang, *Small*, 2024, 2401327.
28 C. Kauany, S. Azevedo, E. Arizono Dos Reis, J. Carlos Germino, J. A. Moreto, A. J. Terezo, E. Fernando and J. Quites, *Quim. Nova*, 2017, **40**, 534–540.
29 N. Nishida, S. Amagasa, Y. Kobayashi and Y. Yamada, *Appl. Surf. Sci.*, 2016, **387**, 996–1001.
30 X. Zhang, H. Xue, J. Sun, N. Guo, T. Song, J. Sun, Y. R. Hao and Q. Wang, *Green Chem.*, 2023, **25**, 8606–8614.
31 W. Jo, D. Jeong, J. Jeong, T. Kim, S. Han, M. Son, Y. Kim, Y. H. Park and H. Jung, *Front. Chem.*, 2021, **9**, 781838.
32 C. Tian, K. Pratama, A. Sharma, M. Watroba, J. Michler and J. Schwiedrzik, *Mater. Sci. Eng., A*, 2024, **897**, 146342.
33 J. Hu, S. Li, J. Chu, S. Niu, J. Wang, Y. Du, Z. Li, X. Han and P. Xu, *ACS Catal.*, 2019, 10705–10711.
34 J. Huang, Y. Li, Y. Zhang, G. Rao, C. Wu, Y. Hu, X. Wang, R. Lu, Y. Li and J. Xiong, *Angew. Chem.*, 2019, **131**, 17619–17625.
35 M. Chen, D. Liu, Y. Chen, D. Liu, X. Du, J. Feng, P. Zhou, B. Zi, Q. Liu, K. H. Lo, S. Chen, S. Wang, W. F. Ip and H. Pan, *Appl. Mater. Today*, 2022, **26**, 101343.
36 K. Li, G. Zhou, Y. Tong, Y. Ye and P. Chen, *ACS Sustain. Chem. Eng.*, 2023, **11**, 14186–14196.
37 Y. Xing, S. Liu, Y. Liu, X. Xiao, Y. Li, Z. Wang, Y. Hu, B. Xin, H. Wang and C. Wang, *Nano Energy*, 2024, **123**, 109402.
38 H. Li, J. Xiang and H. Li, *J. Mater. Sci.: Mater. Electron.*, 2020, **31**, 11425–11433.
39 W. Tang, X. Liu, Y. Li, Y. Pu, Y. Lu, Z. Song, Q. Wang, R. Yu and J. Shui, *Nano Res.*, 2020, **13**, 447–454.
40 S. Liu, Y. Wang, J. Gao, W. Jin, W. Xiao, L. Xin, Z. Xiao, G. Xu, C. Dai, H. Zhang, Z. Wu and L. Wang, *Fuel*, 2024, **367**, 131445.
41 Y. Qiu, Q. Jia, S. Yan, B. Liu, J. Liu and X. Ji, *ChemSusChem*, 2020, **13**, 4911–4915.
42 G. Wang, W. Tang, S. Yang, M. Lu, H. Wei, L. Cui and X. Chen, *J. Mater. Chem. A*, 2023, **11**, 26519–26530.

43 C. Wan, Y. Jiao, T. Qiang and J. Li, *Carbohydr. Polym.*, 2017, **156**, 427–434.
44 B. P. Payne, M. C. Biesinger and N. S. McIntyre, *J. Electron Spectrosc. Relat. Phenom.*, 2009, **175**, 55–65.
45 A. R. Blume, W. Calvet, A. Ghafari, T. Mayer, A. Knop-Gericke and R. Schlögl, *Phys. Chem. Chem. Phys.*, 2023, **25**, 25552–25565.
46 Z. Wu, L. Huang, H. Liu and H. Wang, *ACS Catal.*, 2019, **9**, 2956–2961.
47 D. Y. Chung, S. W. Jun, G. Yoon, H. Kim, J. M. Yoo, K. S. Lee, T. Kim, H. Shin, A. K. Sinha, S. G. Kwon, K. Kang, T. Hyeon and Y. E. Sung, *J. Am. Chem. Soc.*, 2017, **139**, 6669–6674.
48 N. Guo, H. Xue, J. Sun, T. Song, H. Dong, Z. Zhao, J. Zhang, Q. Wang and L. Wu, *Next Mater.*, 2024, **3**, 100109.
49 K. Zhu, W. Luo, G. Zhu, J. Wang, Y. Zhu, Z. Zou and W. Huang, *Chem.–Asian J.*, 2017, **12**, 2720–2726.
50 X. Y. Ji, K. Sun, Z. K. Liu, X. Liu, W. Dong, X. Zuo, R. Shao and J. Tao, *Nano-Micro Lett.*, 2023, **15**, 1–15.
51 T. Zhao, X. Li, J. Hu, J. Zhou, X. Jia and G. Hu, *J. Environ. Chem. Eng.*, 2023, **11**, 110122.
52 S. Anantharaj, S. Noda, V. R. Jothi, S. C. Yi, M. Driess and P. W. Menezes, *Angew. Chem., Int. Ed.*, 2021, **60**, 18981–19006.
53 E. Castañeda-Morales, J. O. Peralta-Cruz, F. Ruiz-Zepeda, A. Susarrey-Arce, M. L. Hernández-Pichardo and A. Manzo-Robledo, *Mater. Today Energy*, 2024, **41**, 101525.
54 W. Liao, J. Wang, G. Ni, K. Liu, C. Liu, S. Chen, Q. Wang, Y. Chen, T. Luo, X. Wang, Y. Wang, W. Li, T. S. Chan, C. Ma, H. Li, Y. Liang, W. Liu, J. Fu, B. Xi and M. Liu, *Nat. Commun.*, 2024, **15**(1), 1–12.
55 A. Richa, S. Touil and M. Fizir, *J. Environ. Manage.*, 2022, **316**, 115265.
56 A. Rahman, N. C. Mondal and K. K. Tiwari, *Sci. Rep.*, 2021, **11**(1), 1–13.
57 J. Li, Y. Zhang, C. Liu, L. Zheng, E. Petit, K. Qi, Y. Zhang, H. Wu, W. Wang, A. Tiberj, X. Wang, M. Chhowalla, L. Lajaunie, R. Yu and D. Voiry, *Adv. Funct. Mater.*, 2022, **32**, 2108316.
58 Y. Wang, L. Zhang, Y. Niu, D. Fang, J. Wang, Q. Su and C. Wang, *Green Chem.*, 2021, **23**, 7594–7608.
59 Y. Guo, R. Zhang, S. Zhang, Y. Zhao, Q. Yang, Z. Huang, B. Dong and C. Zhi, *Energy Environ. Sci.*, 2021, **14**, 3938–3944.
60 Z. Gao, Y. Lai, Y. Tao, L. Xiao, L. Zhang and F. Luo, *ACS Cent. Sci.*, 2021, **7**, 1066–1072.
61 X. Deng, Y. Yang, L. Wang, X. Z. Fu and J. L. Luo, *Adv. Sci.*, 2021, **8**(7), 2004523.
62 Z. Liu, C. Wang, C. Chen, C. Li and C. Guo, *Electrochem. Commun.*, 2021, **131**, 107121.
63 J. Y. Fang, Q. Z. Zheng, Y. Y. Lou, K. M. Zhao, S. N. Hu, G. Li, O. Akdim, X. Y. Huang and S. G. Sun, *Nat. Commun.*, 2022, **13**(1), 7899.
64 Y. Wang, A. Xu, Z. Wang, L. Huang, J. Li, F. Li, J. Wicks, M. Luo, D. H. Nam, C. S. Tan, Y. Ding, J. Wu, Y. Lum, C. T. Dinh, D. Sinton, G. Zheng and E. H. Sargent, *J. Am. Chem. Soc.*, 2020, **142**, 5702–5708.
65 K. Wu, C. Sun, Z. Wang, Q. Song, X. Bai, X. Yu, Q. Li, Z. Wang, H. Zhang, J. Zhang, X. Tong, Y. Liang, A. Khosla and Z. Zhao, *ACS Mater. Lett.*, 2022, **4**, 650–656.
66 F. Y. Chen, Z. Y. Wu, S. Gupta, D. J. Rivera, S. V. Lambeets, S. Pecaut, J. Y. T. Kim, P. Zhu, Y. Z. Finfrock, D. M. Meira, G. King, G. Gao, W. Xu, D. A. Cullen, H. Zhou, Y. Han, D. E. Perea, C. L. Muhich and H. Wang, *Nat. Nanotechnol.*, 2022, **17**(7), 759–767.
67 N. C. Kani, N. H. L. Nguyen, K. Markel, R. R. Bhawnani, B. Shindel, K. Sharma, S. Kim, V. P. Dravid, V. Berry, J. A. Gauthier and M. R. Singh, *Adv. Energy Mater.*, 2023, **13**, 2204236.
68 C. Sun, H. Wang, J. Ren, X. Wang and R. Wang, *Nanoscale*, 2021, **13**, 13703–13708.
69 M. Gong and H. Dai, *Nano Res.*, 2015, **8**, 23–39.
70 Y. Feng, S. Wang, H. Wang, Y. Zhong and Y. Hu, *J. Mater. Sci.*, 2020, **55**, 13927–13937.
71 F. Lei, K. Li, M. Yang, J. Yu, M. Xu, Y. Zhang, J. Xie, P. Hao, G. Cui and B. Tang, *Inorg. Chem. Front.*, 2022, **9**, 2734–2740.
72 S. E. Bae, K. L. Stewart and A. A. Gewirth, *J. Am. Chem. Soc.*, 2007, **129**, 10171–10180.
73 L. R. Sadergaski, T. J. Hager and H. B. Andrews, *ACS Omega*, 2022, **7**, 7287–7296.
74 Z. Qiu, C. W. Tai, G. A. Niklasson and T. Edvinsson, *Energy Environ. Sci.*, 2019, **12**, 572–581.
75 D. P. Butcher and A. A. Gewirth, *Nano Energy*, 2016, **29**, 457–465.
76 J. Theerthagiri, J. Park, H. T. Das, N. Rahamathulla, E. S. F. Cardoso, A. P. Murthy, G. Maia, D.-V. N. Vo and M. Y. Choi, *Environ. Chem. Lett.*, 2022, **20**(5), 2929–2949.
77 X. Wang, C. Xu, M. Jaroniec, Y. Zheng and S. Z. Qiao, *Nat. Commun.*, 2019, **10**(1), 1–8.
78 R. Chen, S. F. Hung, D. Zhou, J. Gao, C. Yang, H. Tao, H. Bin Yang, L. Zhang, L. Zhang, Q. Xiong, H. M. Chen and B. Liu, *Adv. Mater.*, 2019, **31**, 1903909.
79 R. L. Aggarwal, L. W. Farrar, S. Di Cecca and T. H. Jeys, *AIP Adv.*, 2016, **6**, 25310.
80 Y. Peng, K. Li and J. Li, *Appl. Catal. B Environ.*, 2013, **140–141**, 483–492.
81 F. Lei, K. Li, M. Yang, J. Yu, M. Xu, Y. Zhang, J. Xie, P. Hao, G. Cui and B. Tang, *Inorg. Chem. Front.*, 2022, **9**, 2734–2740.
82 H. Liu, X. Lang, C. Zhu, J. Timoshenko, M. Rüscher, L. Bai, N. Guijarro, H. Yin, Y. Peng, J. Li, Z. Liu, W. Wang, B. R. Cuenya and J. Luo, *Angew. Chem., Int. Ed.*, 2022, **61**, e202202556.
83 B. M. Leu, M. Z. Zgierski, G. R. A. Wyllie, W. R. Scheidt, W. Sturhahn, E. E. Alp, S. M. Durbin and J. T. Sage, *J. Am. Chem. Soc.*, 2004, **126**, 4211–4227.
84 D. Bykov and F. Neese, *J. Biol. Inorg. Chem.*, 2012, **17**, 741–760.
85 J. Li, Q. Peng, A. G. Oliver, E. E. Alp, M. Y. Hu, J. Zhao, J. T. Sage and W. R. Scheidt, *J. Am. Chem. Soc.*, 2014, **136**, 18100–18110.
86 T. S. Kurtikyan, A. A. Hovhannisyan, A. V. Iretskii and P. C. Ford, *Inorg. Chem.*, 2009, **48**, 11236–11241.

87 Z. N. Nilsson, B. L. Mandella, K. Sen, D. Kekilli, M. A. Hough, P. Moënne-Loccoz, R. W. Strange and C. R. Andrew, *Inorg. Chem.*, 2017, **56**, 13205–13213.
88 F. Li, Z. Men, S. Li, S. Wang, Z. Li and C. Sun, *Spectrochim. Acta Mol. Biomol. Spectrosc.*, 2018, **189**, 621–624.
89 A. A. Howard, G. S. Tschumper and N. I. Hammer, *J. Phys. Chem. A*, 2010, **114**, 6803–6810.
90 J. Sun, W. Gao, H. Fei and G. Zhao, *Appl. Catal. B Environ.*, 2022, **301**, 120829.
91 O. Elmutasim and S. M. Alhassan, *Ind. Eng. Chem. Res.*, 2021, **60**, 15525–15539.
92 L. Partanen, S. Alberti and K. Laasonen, *Phys. Chem. Chem. Phys.*, 2021, **23**, 11538–11547.
93 P. Zhang, H. Qiu, H. Li, J. He, Y. Xu and R. Wang, *Nanomaterials*, 2022, **12**, 1130.